Nano Research

Open Access

Research Article

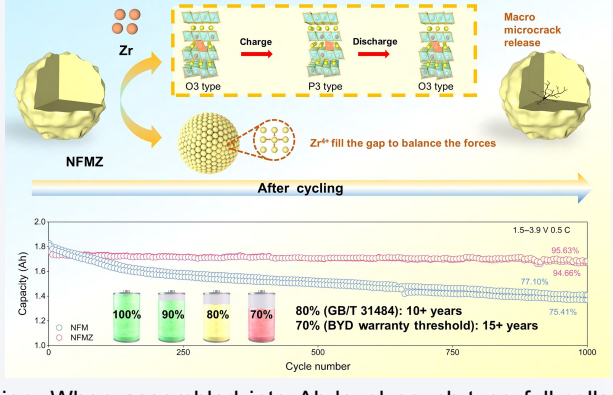
Mitigating irregular stress release in cathode materials to enable long-term cycling of Ah-level sodium-ion pouch cells

Zhongxuan Li[1], Jia Gao[1], Yulu Tian[1], Shaochen Ji[1], Zhichao Xu[1], Liubin Wang[1], Zeheng Li[2] ✉, Min Hong[4], Wenlong Cai[3] ✉, Tianpin Wu[2], Jun Lu[2], and Jixue Shen[1,5] ✉

[1] *College of Chemistry and Materials Science, The Flame Retardant Material and Processing Technology Engineering Research Center of Hebei Province, Hebei University, Baoding 071002, China*
[2] *College of Chemical and Biological Engineering, Zhejiang University, Hangzhou 310058, China*
[3] *College of Materials Science and Engineering, Sichuan University, Chengdu 610064, China*
[4] *Quzhou Institute of Power Battery and Grid Energy Storage, Quzhou 324000, China*
[5] *Key Laboratory of Advanced Energy Materials Chemistry (Ministry of Education), Nankai University, Tianjin 300071, China*

Cite this article: *Nano Research*, **2026**, *19*, 94908806. https://doi.org/10.26599/NR.2026.94908806

ABSTRACT: The O3-type $NaTMO_2$ (where TM represents transition metals) cathode material is highly promising for sodium-ion batteries due to its high theoretical specific capacity and cost-effectiveness. However, its industrialization and commercialization have been hindered by complex phase transitions, sluggish sodium-ion diffusion kinetics, and inhomogeneous stress release within the transition metal layers. In this study, we employ a Zr-doped O3-type $NaNi_{1/3}Fe_{1/3}Mn_{1/3}O_2$ (NFMZ, NFM represents $NaNi_{1/3}Fe_{1/3}Mn_{1/3}O_2$) cathode material to address these challenges. The incorporation of Zr promotes the growth of the (003) crystal plane, accelerates the kinetic process, increases the sodium-ion diffusion coefficient, and enhances the TM–O bond energy, thereby improving phase transition reversibility and enabling a rapid O3-to-P3 transformation. When assembled into Ah-level pouch-type full-cells with a hard carbon anode, the NFMZ cathode delivers an excellent discharge capacity of 1.76 Ah within a voltage range of 1.5–3.9 V at 0.5 C, and retains 95.63% of its initial capacity after 1000 cycles. More importantly, this work elucidates the mechanism by which Zr doping enhances the electrochemical performance of NFM. The NFMZ cathode also exhibits an enhanced stress release mechanism from the interior to the exterior, effectively mitigating stress accumulation and enabling the stable operation of Ah-level pouch-type full-cells.



KEYWORDS: sodium-ion batteries, layer cathode materials, structure stability, stress and strain, Ah-level pouch cells

1 Introduction

With the growing emphasis on energy and environmental issues, the development of new energy sources and the improvement of energy efficiency have become the primary objectives of technological progress in the energy sector [1–5]. In recent years, the rapid development of electric vehicles, portable electronic devices, and energy storage stations has driven substantial demand for lithium-ion batteries (LIBs) [6–8]. However, the limited supply and uneven distribution of lithium resources have raised concerns about raw material scarcity and rapidly increasing costs [9, 10]. Among alternatives, sodium-ion batteries (SIBs), which share similar electrochemical mechanisms with LIBs, are regarded as an important complement to LIBs technology due to their low production cost, environmental sustainability, and high safety [11–14]. As a key component influencing both the production cost and performance of SIBs, it is essential to develop advanced cathode materials with high energy density and long cycle life [15–17]. Layered transition metal (TM) oxides with an O3-type structure (denoted as Na_xTMO_2, where $x \leq 1$) are considered promising cathode materials for commercial SIBs due to their sufficient Na content and high reversible capacity, making them more suitable for practical applications when paired with hard carbon anodes in SIBs [18–21].

Received: April 7, 2026; **Revised:** April 27, 2026
Accepted: May 3, 2026

✉Address correspondence to Jixue Shen, jixueshen@hbu.edu.cn; Wenlong Cai, caiwl@scu.edu.cn; Zeheng Li, zehengli@zju.edu.cn

However, O3-type sodium-ion cathode materials are hindered by complex phase transitions and sluggish Na^+ diffusion kinetics [22–24]. Intricate phase transformations, accompanied by significant changes along the *c*-axis, lead to the collapse of the layered structure and severe capacity degradation. The complex transitions among O3, P3, and related phases result in substantial volume variations, inducing considerable lattice strain [25–27]. These irregular strains disrupt the layered structure and reduce cycling stability. The slow Na^+ diffusion kinetics cause uneven distribution of sodium ions within the particles, leading to the accumulation of internal stress [28]. The difference in ion diffusion kinetics between the bulk and surface results in an inhomogeneous sodium ion concentration gradient, generating uneven stress between the surface and interior, which promotes the formation of microcracks [29]. Ultimately, the complex phase transitions and slow Na^+ diffusion kinetics in O3-type cathode materials lead to the accumulation of irregular stresses during cycling. These stresses damage the layered structure, impair cycling stability, and the irregular stress release within the transition metal layer poses a challenge to the industrial production and commercial application of SIBs [30, 31].

To enhance the cycling stability of O3-type layered oxide materials, numerous efforts have been made, including surface engineering [32–34], multiphase structure design [35–37], and elemental doping [38–41]. Unlike the first two strategies, which are hindered by complex synthesis processes, elemental doping offers an efficient and scalable approach to improve the performance of cathode materials under high voltage. Cationic element doping includes low-valence doping [42], medium-valence doping [43], and high-valence doping [44]. Among these, high-valence metal ion doping can effectively enhance the bond energy of TM–O, expand the *c*-axis of the material, and improve the reversibility of phase transitions, thereby strengthening the structural stability of O3-type sodium-ion cathode materials during the interlayer sliding process associated with complex phase transitions [45]. However, previous studies have not addressed how high-valence metal ion doping influences the generation and accumulation of inhomogeneous stress and strain within the cathode material.

In this study, a novel cathode material, NFMZ, was successfully designed by incorporating Zr into $NaNi_{1/3}Fe_{1/3}Mn_{1/3}O_2$ (NFM). The ionic radius and bond energy of Zr^{4+} are larger than those of Ni^{2+}, Fe^{3+}, and Mn^{4+}. The introduction of Zr leads to an increased crystallite size of the (003) plane during material preparation, expanding the interlayer spacing along the *c*-axis and facilitating Na^+ insertion/extraction. This enhances lattice stability during phase transitions and improves the stress release mechanism. This strategy not only improves the structural stability of the O3-type material but also enhances the reversibility of phase transformations. In this work, the Zr-doped NFMZ exhibits excellent electrochemical performance, particularly in terms of cycling stability. When assembled into Ah-level pouch-type full-cells and cycled within a voltage range of 1.5–3.9 V at a rate of 0.5 C, NFMZ achieves a high-capacity retention of 95.63% after 1000 cycles, demonstrating outstanding capacity retention capability. These performance enhancements are attributed to the Zr doping, which accelerates Na^+ migration, reduces polarization, and enhances structural stability and the stress release mechanism. The reduced energy barrier for Na^+ migration, mitigated lattice expansion/contraction, more uniform stress release, and reduced lattice cracking collectively contribute to accelerated kinetics and significantly improved electrochemical performance. This study elucidates the mechanism by which Zr doping improves the stress release mechanism of NFM cathode materials for sodium-ion batteries and provides unique insights into enabling the application of Ah-level sodium-ion pouch cells through enhanced stress release.

2 Results and discussion

2.1 Preparation procedure and structure analysis

Figure 1(a) illustrates the preparation flowchart for the NFMZ cathode material. The precursor was first prepared via a co-precipitation method, which was then thoroughly mixed with Na_2CO_3 and ZrO_2, followed by high-temperature calcination. The addition of Zr enhances sintering and mass transport during calcination, resulting in the enlargement of primary particles and more uniform aggregation within secondary particles. Inductively coupled plasma-optical emission spectrometry (ICP-OES) was performed to verify the overall composition, as presented in Table S1 in the Electronic Supplementary Material (ESM), which closely aligned with the intended molar ratios of the various metal elements. Subsequently, the scanning electron microscopy (SEM) image of the NFMZ material (Fig. 1(b)) reveals its polycrystalline morphology. Compared to NFM particles (Figs. S1 and S2 in the ESM), the introduction of Zr in NFMZ results in more regularly grown primary particles and the formation of relatively stable spherical secondary particles. In contrast, the primary particles of NFM grow more disorderly, leading to irregularly shaped secondary particles (Fig. 1(c)). The secondary particle size distribution in the NFMZ material (Fig. 1(d)) more closely follows a Gaussian distribution, indicating more uniform particle growth. This is similar to the previous reports on lithium-ion batteries [46]. The addition of Zr leads to a more thorough and synchronized recrystallization and growth process within each secondary particle of NFMZ, leading to a convergence of secondary particle sizes towards a more centralized average value. As a result, the particle size distribution becomes more normal and shows increased size uniformity. The concentrated and uniform particle size distribution of NFMZ implies that the particles can achieve tighter and more uniform packing within the electrode. During charging/discharging cycles, mechanical stress can be distributed more evenly across the entire electrode, avoiding local stress concentration and enhancing the structural stability of the material.

To analyze the crystal structure of the samples, X-ray powder diffraction (XRD) patterns were performed, with the results shown in Fig. S3 in the ESM. The diffraction peaks for both samples correspond to an O3-type α-$NaFeO_2$ structure with a hexagonal lattice (space group $R\bar{3}m$) [47]. Distinct characteristic peaks were observed in all samples, confirming the excellent crystallinity of the materials. Energy-dispersive X-ray spectroscopy (EDS) analysis (Fig. 1(e)) confirmed the successful incorporation of Zr into the NFM material. Furthermore, Zr doping enabled multi-dimensional crystal plane regulation, effectively promoting the growth of crystallite size for the (003) plane (Fig. 1(f)). The (003) plane runs parallel to the layered planes, so an increase in its size (determined using the Scherrer equation) indicates a longer coherent crystal length in this direction. This suggests a reduction in internal defects, dislocations, and grain boundaries, pointing to more complete and superior-quality crystals. Within larger crystallites, stress propagation encounters fewer obstacles like grain boundaries and

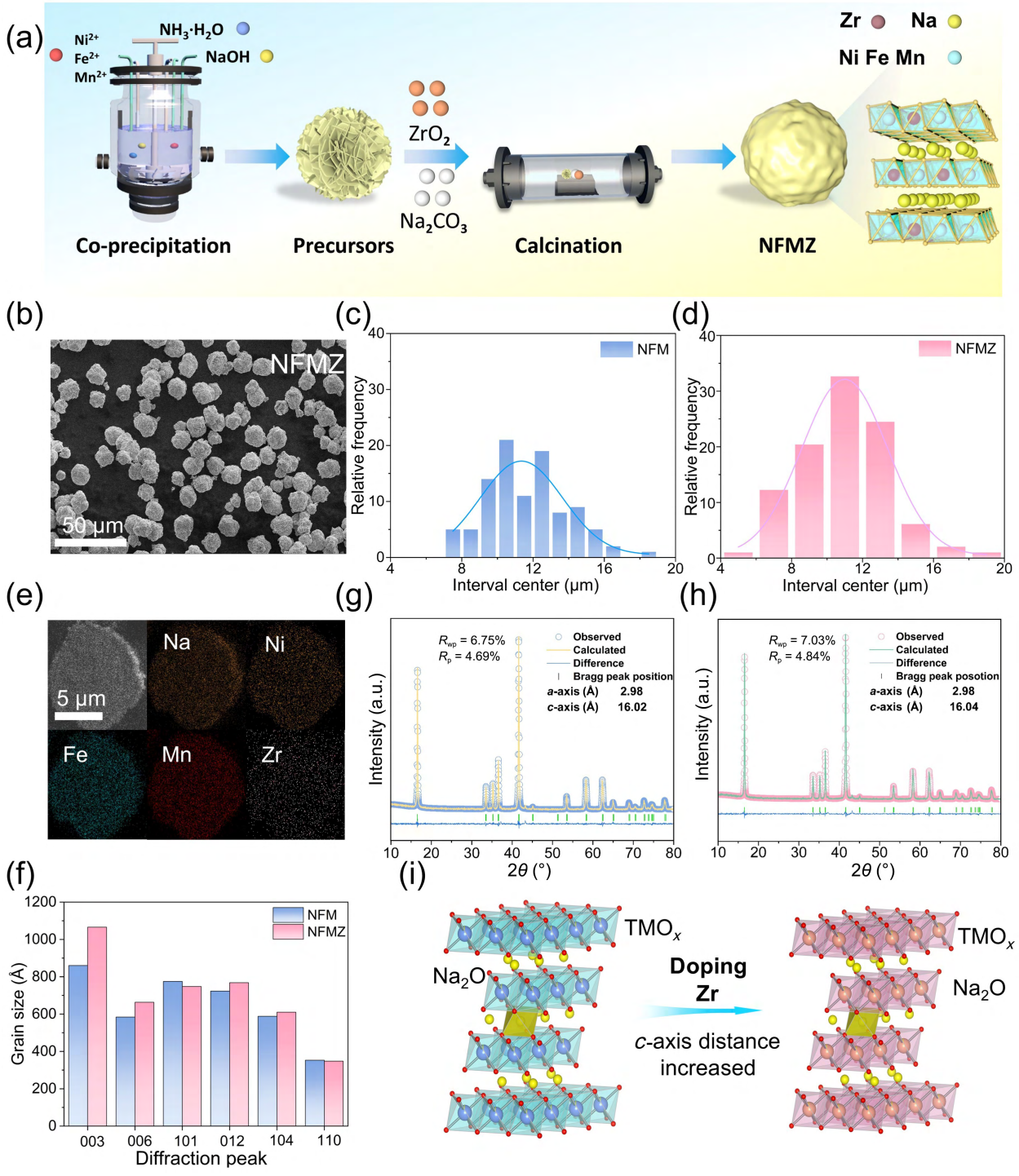


Figure 1 (a) Flowchart of NFMZ material preparation. (b) SEM image of the NFMZ cathode material. Secondary particle size distribution of the (c) NFM and (d) NFMZ materials. (e) EDS mapping of NFMZ. (f) Crystallite size of different crystal planes for the NFMZ material. Rietveld refinement of the *in situ* XRD patterns for the (g) NFM and (h) NFMZ. (i) Schematic illustration of the crystal structure for the synthesized Zr-doped cathode material.

defects. Consequently, microscopic stress distribution becomes more uniform, is less likely to concentrate at grain boundaries and initiate microcracks, and provides better resistance to the structural distortion stress induced by sodium-ion extraction/insertion. To further verify the changes in displacement and lattice parameters, Rietveld refinement was performed on the XRD patterns of the different samples, as shown in Figs. 1(g) and 1(h). The doping of Zr expands the *c*-axis of the material, making it easier for sodium ions to migrate [48]. Detailed data provided in Tables S2 and S3 in the ESM confirm that Ni, Mn, Zr, and Fe occupy the transition metal sites. Additionally, Fig. 1(i) illustrates the evolution of the crystal structure of the NFM cathode material before and after Zr doping. As shown, the material consists of alternating layers of TMO_2 octahedra and Na layers. With the introduction of Zr, the lattice parameter c increases, indicating partial substitution within the bulk structure, which affects the lattice arrangement.

2.2 Electrochemical performance

The electrochemical performance of NFMZ and NFM cathodes was investigated using coin-type half-cells. After 250 cycles at 1 C, NFMZ retained 82.1% of its capacity, while NFM retained only 66.6% (Fig. 2(a)). At 10 C and after 250 cycles, NFMZ retained 69.6% of its capacity, whereas NFM retained only 5.3% (Fig. 2(b)). This indicates that the layered structure of NFM may collapse under high-rate long-term cycling, hindering Na^+ migration and slowing diffusion kinetics, resulting in rapid capacity decay. In contrast, NFMZ exhibited smaller capacity decay at 10 C, maintaining a good layered structure during long-term cycling. To further investigate capacity changes during cycling, comparative tests were conducted. After 280 cycles, NFMZ delivered a capacity of 108.2 mAh·g^{-1} at 1 C, equivalent to 78.9% of its initial capacity. On the other hand, NFM showed a reversible discharge capacity of 102.3 mAh·g^{-1}, approximately 74.3% of its initial capacity. The enhanced cycling performance of NFMZ is significantly better than that of NFM. After 280 cycles, NFMZ maintained 82.4% of its discharge capacity, while NFM maintained only 56.0% under the same conditions (Fig. S4 in the ESM). This can be attributed to Zr doping enhancing structural stability, improving the reversibility of phase transitions, and ameliorating the stress release mechanism, thereby enhancing cycling stability.

The irreversible phase transitions in NFM are often accompanied by incomplete or unstable electrochemical reactions, reducing active sites and thus decreasing the material's capacity—a common issue with NFM cathode materials. NFMZ exhibited good stability even under high-rate charge/discharge performance. As shown in Fig. 2(c), NFMZ gradually demonstrated a significant advantage as the rate increased, showing higher capacities than NFM at high rates of 5 and 10 C. Furthermore, the charge/discharge curves of NFMZ and NFM at different rates (Fig. S5 in the ESM) further

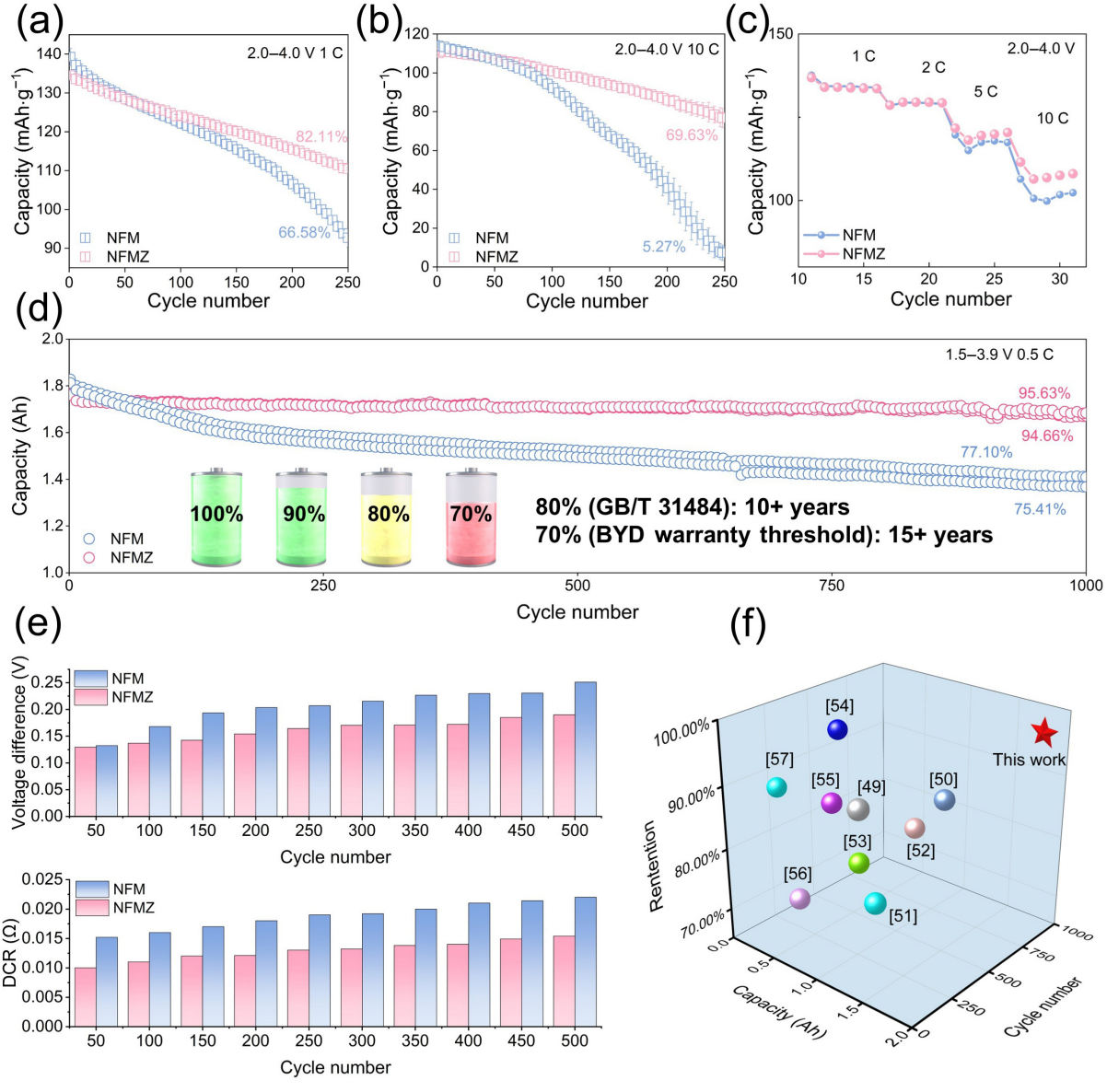


Figure 2 Performance comparison of coin-type half-cells cycled 250 cycles at (a) 1 C and (b) 10 C within a voltage range of 2.0–4.0 V. (c) Rate capability comparison of NFM and NFMZ within the voltage range of 2.0–4.0 V. (d) Performance comparison of pouch-type cells 1000 cycles at 0.5 C within a voltage range of 1.5–3.9 V. (e) Comparison of voltage difference and DCR (direct current discharge resistance) for NFMZ and NFM. (f) Electrochemical performance comparison between the results reported previously and this work for cathode materials.

illustrate that with increasing rate, the voltage stability and capacity retention of NFMZ are superior to those of NFM. This is likely because the layered structure of NFM is damaged under high rates, leading to performance degradation, whereas Zr doping in NFMZ helps maintain the layered structure, improves the release of uneven stress, and thus preserves good electrochemical performance.

To further explore the commercial feasibility of NFMZ, pouch-type full-cells with a hard carbon anode were designed (Table S4 in the ESM) and tested electrochemically within a voltage range of 1.5–3.9 V. After 1000 cycles at 0.5 C, NFMZ retained 95.63% of its initial discharge capacity, with a final capacity of 1.68 Ah (Fig. 2(d)). In contrast, NFM showed significant performance degradation, with a final capacity of 1.37 Ah. We observed that NFMZ pouch cells exhibit a long cycle life, with energy showing an approximately linear decline. We performed a linear fit and calculated the number of cycles when the capacity fades to 80% and 70% of its initial value. According to the national standard GB/T 31484 and BYD's warranty threshold, and considering one cycle per day for commercial vehicles, it can be estimated that the service life of new energy vehicles equipped with this cathode material is approximately 10 years or more, and 15 years or more.

Additionally, NFMZ exhibited a smaller median voltage difference and lower direct current resistance (DCR). The midpoint voltage difference between charge and discharge processes and the DCR for each cycle are shown in Fig. 2(e). After 500 cycles, the voltage hysteresis of NFMZ (~ 0.06 V) was significantly lower than that of NFM (~ 0.12 V), indicating reduced polarization during cycling. This suggests that compared to NFM, the structural stability of NFMZ is maintained more effectively over time, resulting in less resistance accumulation. Furthermore, the DCR of NFMZ was consistently lower than that of NFM, underscoring its superior electrochemical stability. Comparative data (Fig. 2(f) and Table S5 in the ESM) further indicate that NFMZ exhibits superior capacity retention under long-term cycling compared to other sodium-ion battery cathode materials [49–57]. Therefore, in long-term cycling of pouch cells, the Zr-doped NFMZ material demonstrates better electrochemical performance.

2.3 Electrochemical kinetics and finite element analysis

The diffusion rates of Na^+ during charging and discharging are shown in Figs. 3(a) and 3(b). The results show that the average diffusion coefficient of Na^+ in NFMZ is approximately one order of magnitude higher than in pristine NFM, which correlates well with the previously discussed characterization results. The improved kinetics of NFMZ can be attributed to the promoted growth of the (003) plane after Zr doping, which expands the *c*-axis and facilitates more favorable Na^+ de/intercalation during charge/discharge [58]. Furthermore, the diffusion kinetics of NFM and NFMZ were systematically studied using the galvanostatic intermittent titration technique (GITT). The diffusion coefficient (D) was calculated using Eq. (1)

$$D = \frac{4}{\pi\tau}\left(\frac{m_B V_m}{M_B S}\right)^2\left(\frac{\Delta E_s}{\Delta E_\tau}\right)^2 \quad (1)$$

where m_B is the mass of the active materials, V_m is the molar volume, M_B is the molecular weight, S is the contact area between electrode and electrolyte, ΔE_s and ΔE_τ are the steady-state voltage difference for the rest and total transient voltage difference after charging for time (τ), respectively, and τ refers to charging or discharging time.

The reaction kinetics of NFM and NFMZ electrodes were investigated using electrochemical impedance spectroscopy (EIS) and GITT techniques. The GITT curves for pristine NFM and Zr-doped NFMZ during charge/discharge, along with the calculated Na^+ diffusion coefficients, are shown in Fig. 3(c). The intrinsic properties of NFM, including its sodium diffusion pathways and smaller *c*-axis, contribute to its poor rate performance. In contrast, NFMZ exhibits a two-dimensional Na^+ transport channel, effectively reducing electrode polarization and increasing the sodium-ion diffusion rate. Concentration and stress distribution simulations were performed using COMSOL Multiphysics. A geometric model from the COMSOL website was used, with diffusion coefficients derived from GITT calculations. Figures 3(d) and 3(e) show the concentration distribution and stress distribution diagrams for NFM and NFMZ at a state of charge (SOC) of 50% (left: NFM and right: NFMZ). From Fig. 3(d), it can be seen that Zr doping significantly improves the diffusion performance of NFMZ, exhibiting a smaller concentration gradient and more uniform concentration distribution, allowing better Na^+ migration during the discharge process. It is evident that the stress distribution in NFMZ is much smaller than in NFM (Fig. 3(e)). Zr doping reduces the stress generated by volume changes due to Na^+ migration, alleviating stress not only within the particles but also at the grain boundaries. This is likely because Zr doping fills numerous vacancies at the grain boundaries, enhancing structural stability and improving the stress release mechanism. Zr doping helps maintain good contact between active particles, enabling good charge transfer throughout the electrode domain and resulting in smaller and more uniform stress changes between cathode particles.

Typically, the Nyquist plot includes a high-frequency intercept on the *x*-axis representing the Ohmic resistance, two semicircles corresponding to the interface resistance and charge transfer resistance (R_{ct}), and a low-frequency Warburg impedance related to ion diffusion. Among these, R_{ct} plays a pivotal role in the electrochemical reaction, directly relating to the reversibility of the redox process at the electrode/electrolyte interface, and is a key parameter for evaluating the electrochemical performance of the material [59]. The impedance values of NFMZ were significantly reduced compared to pristine NFM. Notably, after 100 and 300 cycles, the impedance of NFMZ (Fig. 3(f) and Fig. S6 in the ESM) remained significantly lower than that of conventional NFM, indicating improved charge transfer kinetics. Cyclic voltammetry (CV) measurements at different scan rates provided valuable insights into the Na^+ diffusion kinetics of NFM and NFMZ in the first cycle (Fig. S7 in the ESM) and the 100th cycle. Within the voltage range of 2.0–4.0 V, as the scan rate increased from 0.2 to 0.8 mV·s^{-1}, the cathodic peak shifted towards lower potential and the anodic peak towards higher potential. In the first cycle, the oxidation/reduction polarization value of NFMZ was 81 mV higher than that of NFM, reflecting enhanced electrochemical kinetics. Notably, phase transition reactions at higher voltages tend to impair the structural stability of the material, causing irreversible damage. After 100 cycles, a similar trend remained (Fig. 3(g)), with the polarization value of the Zr-doped sample exceeding that of NFM by 61 mV, indicating improved structural stability under high-voltage cycling conditions.

2.4 Structural evolution

To investigate the structural evolution of the materials during charge and discharge cycles, *in situ* XRD patterns were performed (Figs. 4(a) and 4(b) and Figs. S8 and S9 in the ESM). At

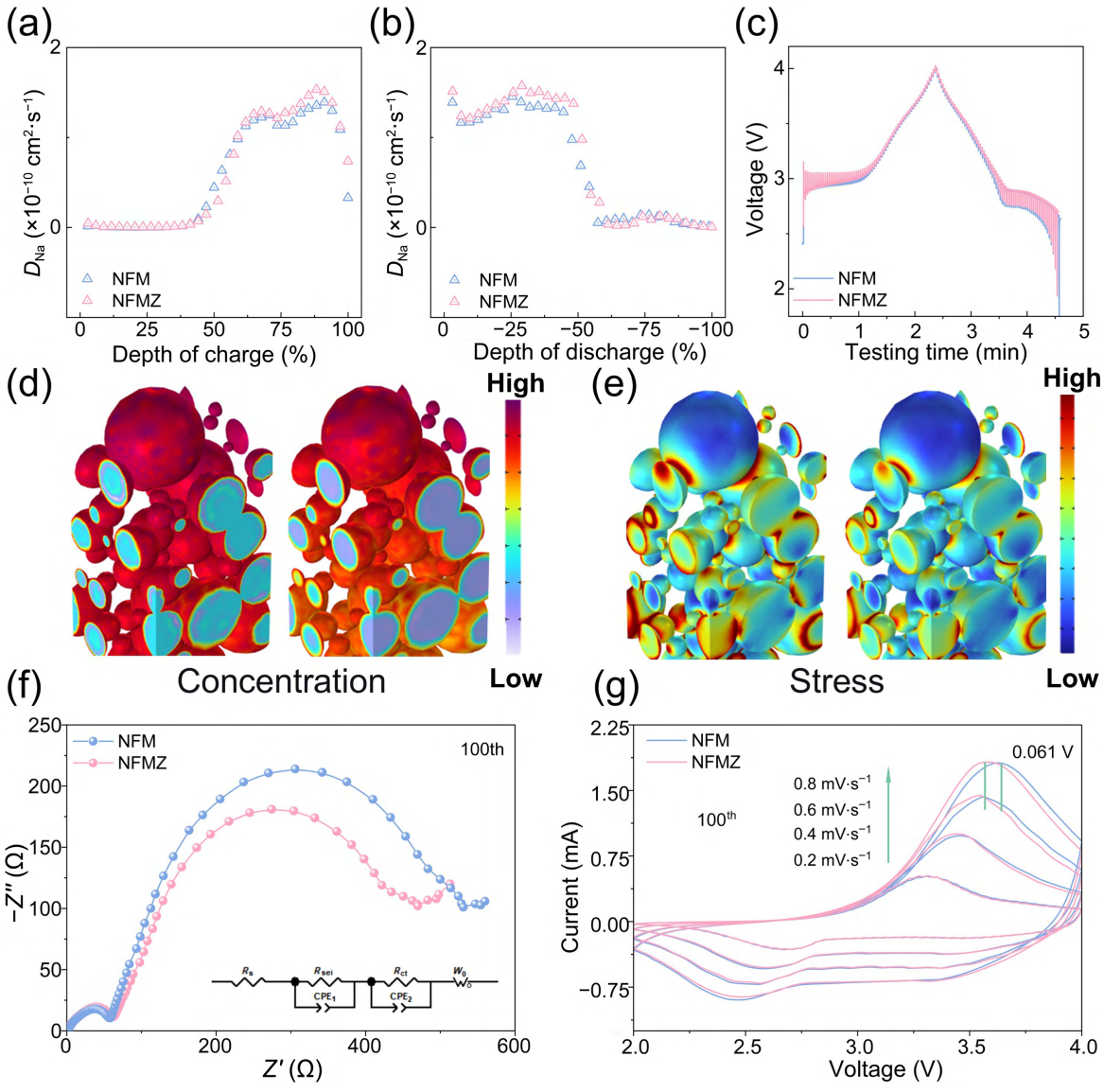


Figure 3 Comparison of calculated Na^+ diffusion coefficient during charging/discharging for (a) NFM and (b) NFMZ. (c) GITT curves for NFM and NFMZ during the initial charge/discharge process. COMSOL simulation of (d) concentration distribution and (e) stress distribution for NFM (left) and NFMZ (right) at 50% SOC. (f) EIS of NFM and NFMZ after 100 cycles. (g) CV curves of NFM and NFMZ at different scan rates after 100 cycles.

the beginning of charging, the (003) peaks of both materials gradually shift to lower angles, indicating that the lattice parameter c increases due to interlayer expansion. This expansion is caused by the enhanced electrostatic repulsion between adjacent oxygen layers [23]. Both materials undergo a phase transition from O3 to P3. A splitting of the (003) peak is observed during charging for each sample, which can be attributed to the thermodynamic preference, at certain sodium concentrations, for the system to separate into two distinct phases with fixed compositions (O3 and P3), rather than forming a compositionally uniform but highly distorted single phase. This separation results in a reduction of the overall free energy, manifesting as a splitting of the (003) diffraction peak. For NFM material, the *in situ* XRD (003) diffraction peak exhibits a significant overlapping region during the charging process (Fig. 4(a)). Under this coexistence of two phases, the substantial difference in lattice constants (especially the *c*-axis) between the old and new phases generates considerable lattice mismatch stress within the grains and between particles. The accumulation and release of this stress are irregular, making it highly prone to initiating microcracks at the phase interfaces, which damages the structural integrity of the particles and consequently leads to the degradation of cycling performance. The evolution of the lattice parameter a provides further evidence. The abrupt drop in the *a*-axis of NFM within the phase transition range further confirms the discontinuous nature of the structural evolution. In contrast, for the Zr-doped NFMZ material, the two-phase coexistence region is narrowed, and the phase transition process becomes more rapid and continuous (Fig. 4(b)). This indicates a reduction of the sharp interfaces between the old and new phases, thereby significantly mitigating the internal stress caused by lattice mismatch and enhancing the structural stability. This behavior is likely due to the Zr doping, which promotes crystallite growth along the (003) plane and expands the *c*-axis parameter. These modifications enhance sodium-ion diffusion kinetics, reduce interfacial resistance, and improve overall reaction kinetics, thereby accelerating the phase transition. In contrast, the extended two-phase coexistence in NFM

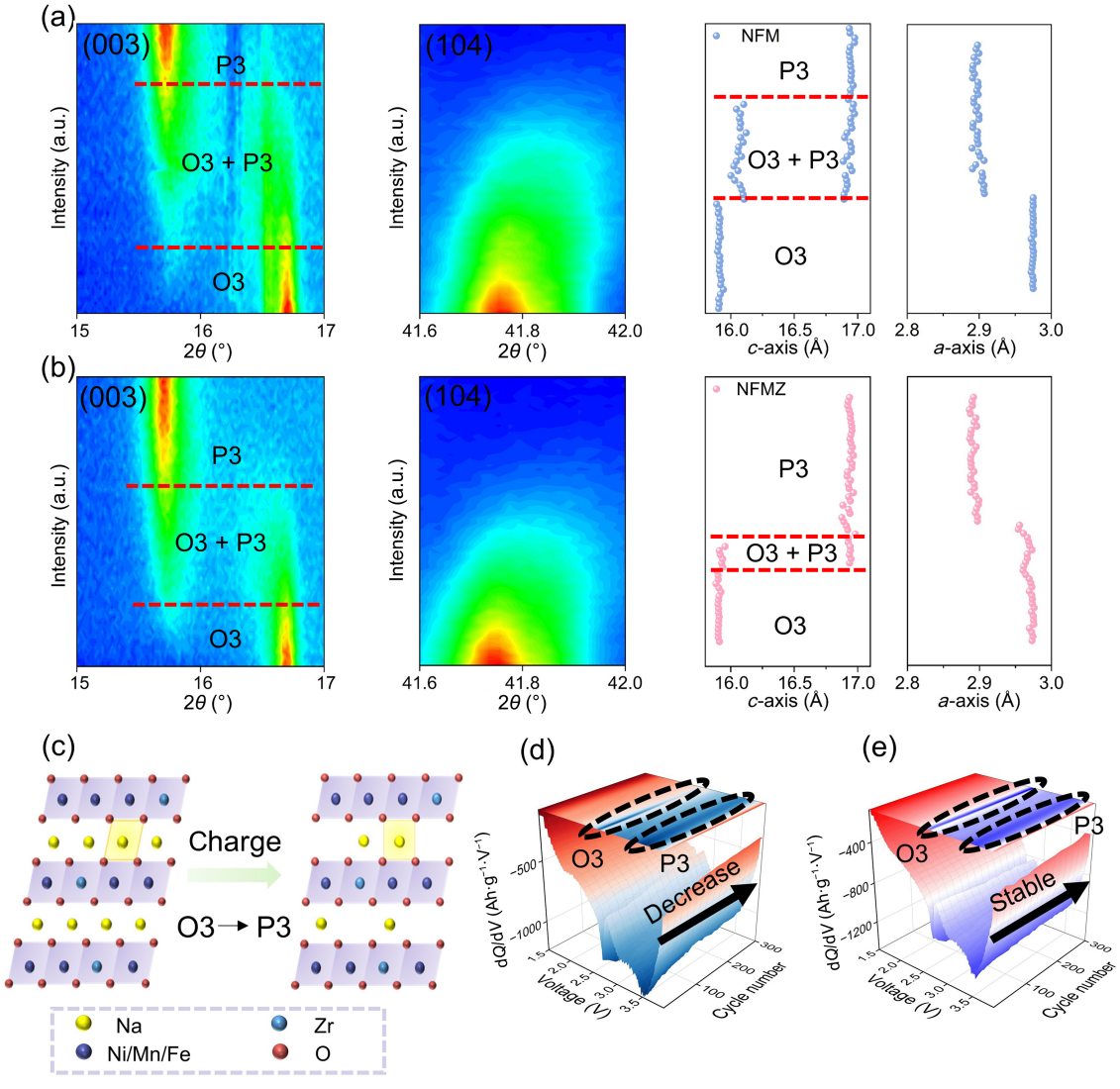


Figure 4 *In situ* XRD patterns of the (003) and (104) diffraction peaks and lattice parameters evolution of *a* and *c* for (a) NFM and (b) NFMZ. (c) Schematic of the structural evolution of NFMZ during charging. (d) d*Q*/d*V* curves of NFM and (e) NFMZ versus cycle number.

indicates greater kinetic barriers and higher energy required for phase boundary migration. The sluggish phase transformation can lead to inhomogeneous reaction progress, where regions of the material exist in different phases simultaneously. This inhomogeneity induces significant internal stresses, which can cause particle cracking, layered structure collapse, and exposure of new surfaces to the electrolyte. These degradation mechanisms promote side reactions and ultimately lead to rapid capacity fade.

A schematic illustration of the rapid phase transformation in NFMZ is presented in Fig. 4(c). Although phase transformation is generally accompanied by substantial volume changes, Zr doping facilitates a faster transition and *c*-axis expansion, which reduces the net volume change and mitigates stress accumulation. As a result, the structural integrity of the layered framework is preserved, contributing to superior electrochemical performance. To further probe the structural changes and capacity fading mechanisms, differential capacity (d*Q*/d*V*, where *Q* represents capacity and *V* represents voltage) curves were analyzed. NFM shows a gradual disappearance of this reversibility with cycling (Fig. 4(d)). NFMZ maintains a reversible O3–P3 phase transition throughout long-term cycling during discharge (Fig. 4(e)). This suggests that the repetitive phase transitions in NFM induce irregular stress accumulation, leading to mechanical degradation and collapse of the layered structure. The irreversible phase behavior accelerates structural deterioration and capacity loss. In contrast, Zr doping in NFMZ enhances the reversibility of the phase transition, alleviates stress concentration, improves stress dissipation, and helps maintain structural stability during extended cycling, thereby achieving improved electrochemical performance.

In summary, Zr doping in NFMZ facilitates faster phase transformation kinetics, shortens the two-phase coexistence region, and improves the reversibility of phase transitions. These changes promote more uniform and efficient stress release, thereby enhancing the structural stability of the material.

2.5 X-ray photoelectron spectroscopy (XPS) analysis and structural comparison

We conducted XPS analysis on the pristine NFM and NFMZ cathode materials. A comparison between Figs. 5(a) and 5(b) indicate a lower content of C–O bonds in NFMZ compared to

NFM. This suggests that Zr doping facilitates the formation of stronger and more stable bonds with surface oxygen, thereby suppressing the release of lattice oxygen and reducing surface reactivity. Consequently, fewer side reactions take place, resulting in a reduced amount of C–O bonds relative to NFM. In contrast, the content of C=O bonds remains nearly identical between NFMZ and NFM, likely due to the higher bond energy and greater chemical inertness of C=O bonds, which render them less sensitive to alterations in the chemical environment induced by doping. The presence of C–C bonds is presumably attributable to the carbonization of organic solvents during high-temperature synthesis. Post-cycling XPS analysis of both materials was also performed. As shown in Figs. 5(c) and 5(d), NFMZ exhibits reduced carbonate formation on its surface compared to NFM. This observation can be ascribed to the stabilization of lattice oxygen and lowered surface activity resulting from Zr doping, which mitigates the reaction with atmospheric CO_2 and thus suppresses carbonate generation [60]. These findings indicate that Zr doping contributes to enhanced structural stability in NFMZ.

Cross-sectional analysis offers direct visualization of the internal morphology of the materials. Prior to cycling (Fig. 5(e)), the untreated NFM material contains evident internal voids, which negatively impact its overall cycling performance. These voids compromise structural integrity, leading to irregular collapse after extended cycling. In contrast, Zr doping (Fig. 5(f)) effectively eliminates these voids, improving the structural coherence and providing a more uniform foundation for stress distribution. Furthermore, this modification promotes the formation of more consistent strain-induced cracks. As depicted in Figs. 5(g) and 5(h), prolonged cycling induces irregular cracks of varying depth and width in NFM, originating from internal voids and propagating outward. The accumulation of these cracks further leads to surface

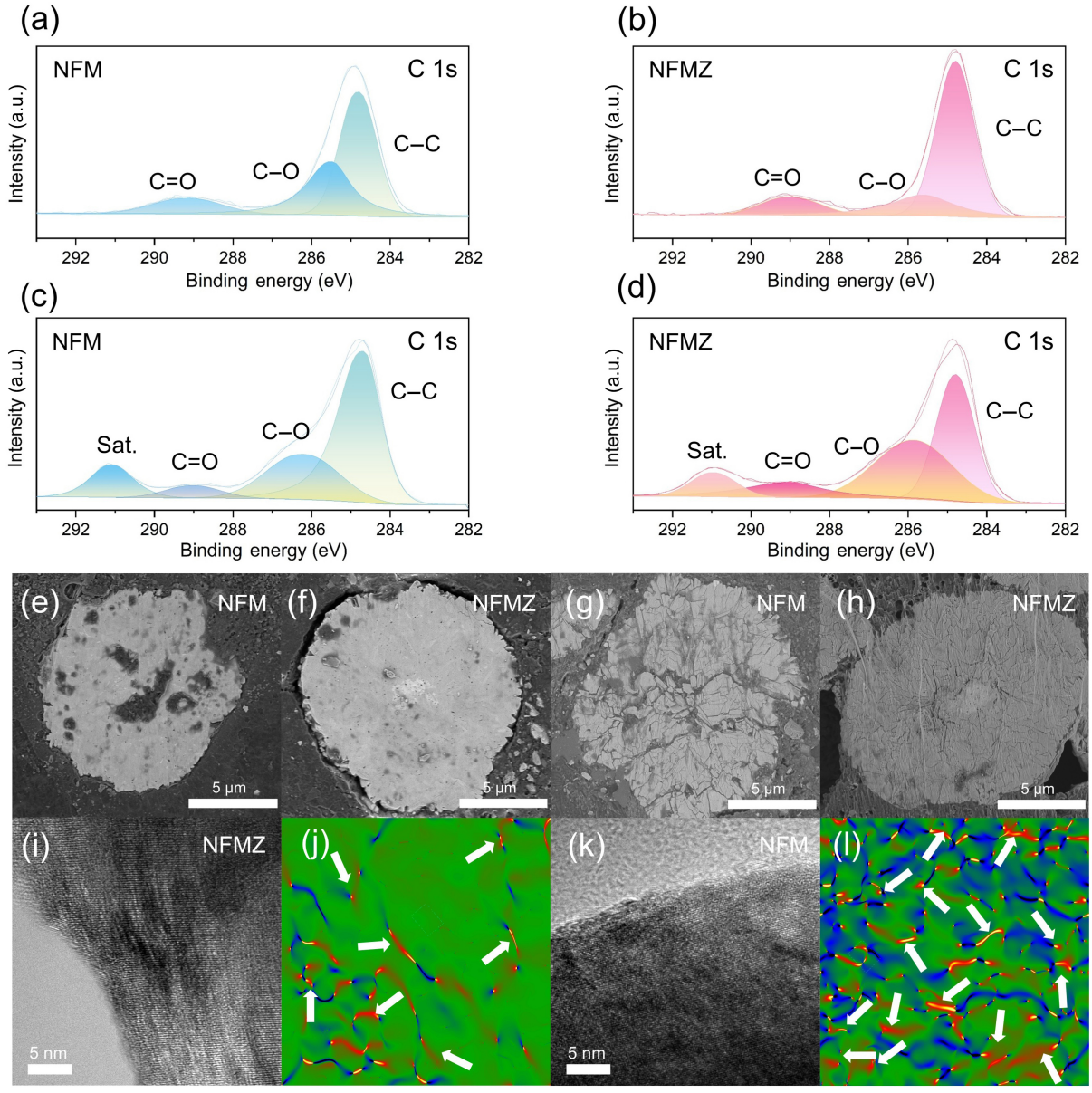


Figure 5 XPS spectra of (a) NFM and (b) NFMZ cathode materials before cycling. XPS spectra of (c) NFM and (d) NFMZ cathode materials after cycling. Cross-sectional SEM images of (e) NFM and (f) NFMZ cathode materials before cycling. Cross-sectional SEM images of (g) NFM and (h) NFMZ cathode materials after cycling. (i) TEM image of cycled NFMZ and (j) the corresponding GPA analysis. (k) TEM image of cycled NFM and (l) the corresponding GPA analysis.

passivation and the interruption of Na charge transport, blocking the Na transport pathways. Under the same cycling conditions, the Zr-doped material also develops cracks, but these are more uniform in morphology. This suggests that Zr incorporation facilitates a more ordered stress accumulation process, with cracks initiating near the center and propagating symmetrically in multiple directions.

To further evaluate post-cycling strain, we performed transmission electron microscopy (TEM) examinations. Figure 5(i) presents a TEM image of cycled NFMZ, and the corresponding geometric phase analysis (GPA) in Fig. 5(j) reveals a relatively uniform strain distribution with minimal irregular deformation. In comparison, the TEM image and GPA mapping of cycled NFM (Figs. 5(k) and 5(l)) show pronounced and irregular strain localization, likely arising from grain boundaries and intra-particle defects in the polycrystalline NFM structure. Such inhomogeneous strain contributes to particle fragmentation and accelerated degradation of structural stability. Analysis of the selected region in Fig. 5(l) further confirms the highly disordered strain pattern in NFM (Fig. S10 in the ESM). In comparison, additional analysis of the selected area (Fig. S11 in the ESM) corroborates the homogeneity of strain in NFMZ. Through Zr doping, we effectively suppressed irregular strain development, thereby significantly improving the structural stability of the material.

2.6 Neutron diffraction and density functional theory (DFT) calculations

To further investigate the effect of Zr doping on the structural stability of the material, neutron powder diffraction was performed. Figures 6(a) and 6(b) present the neutron diffraction results for NFM and NFMZ, respectively. Owing to the larger ionic radius of Zr, Zr doping elongates the O–TM–O bonds, which is manifested as a slight expansion along the *c*-axis and a widening of the sodium-ion diffusion channels. This helps alleviate volume changes during the diffusion process. Additionally, Zr doping increases the overall TM–O bond energy in the material, which is conducive to maintaining the stability of interlayer sliding during phase transitions, thereby enhancing structural stability.

Subsequently, to gain a deeper understanding of the fundamental reasons behind the improved material stability induced by Zr ions, DFT calculations were conducted, as shown in Fig. 6(c). Since the density of states near the Fermi level is primarily contributed by the Ni/Fe/Mn elements, it indicates that the redox center remains unchanged. Therefore, the material's capacity is expected to be well preserved and will not significantly decrease due to Zr doping, while the introduction of Zr stabilizes the overall electronic structure. The Zr-doped material NFMZ retains the original metallic conductivity and redox characteristics, enhancing the overall cycle life and improving the structural stability of the material without sacrificing electrochemical capacity [38].

The optimized crystal structures of the NFM and NFMZ cathodes are shown in Fig. 6(d). Figure 6(e) displays the calculated electron localization function (ELF) maps, which assess the degree of charge localization around each atom. It is evident that the altered distribution of free electrons around O in NFMZ suggests that local electrons undergo electrostatic attraction near O sites due to doping with high-valence metal ions. A comparison of the ELF within the transition metal layers reveals enhanced electron density disorder, which complicates the detachment of lattice oxygen from the host layered structure [61]. This further corroborates the stronger TM–O covalent bonding interactions, thereby reinforcing the structural stability of the material and mitigating irregular stress release.

2.7 Mechanism diagram

A systematic analysis and summary of stress generation and release mechanisms in both NFM and NFMZ are presented, offering clearer insights from the viewpoints of crystal structure evolution and primary particle packing (Fig. 7). From the viewpoint of crystal structure evolution, Zr doping in NFMZ promotes crystallite growth along the (003) plane, expands the interlayer spacing along the *c*-axis, and enhances the reversibility of the O3–P3 phase transition. This accelerates phase transformation kinetics, facilitates more reversible sodium ion insertion/extraction, and promotes interlayer sliding during phase transition. This reduces stress accumulation, improves structural stability, and enhances electrochemical performance over long-term cycling. In contrast, NFM exhibits a smaller *c*-axis spacing, hindering interlayer sliding during phase transformation and resulting in higher energy barriers. After prolonged cycling, weakened P3–O3 phase transitions are observed in NFM, indicating structural degradation, irregular stress, particle cracking, collapse of the layered framework, and deterioration of electrochemical performance.

3 Conclusions

In summary, we have successfully synthesized a Zr-doped O3-type NFMZ cathode material. In the pristine NFM, Na^+ insertion/extraction and the O3–P3 phase transition lead to localized stress accumulation. The irregular release of this stress can cause structural degradation, adversely affecting performance and cycle life. Zr doping significantly enhances the mechanochemical compatibility among the constituent elements, improves Na^+ diffusion kinetics, promotes reversible phase transitions, and achieves more uniform primary particle packing. COMSOL simulations and DFT calculations further confirm the enhanced structural stability of the modified NFMZ material. Concurrently, the NFMZ material exhibits excellent electrochemical performance in Ah-level pouch-type full cells paired with a hard carbon anode, retaining 95.63% of its capacity after 1000 cycles at 0.5 C. This study elucidates the mechanism by which Zr doping improves stress release and provides insights for enhancing the long-term cycling of Ah-level sodium-ion pouch cells.

Electronic Supplementary Material: Supplementary material (further experiments and specific data) is available in the online version of this article at https://doi.org/10.26599/NR.2026.94908806.

Data availability

All data needed to support the conclusions in the paper are presented in the manuscript and the Electronic Supplementary Material. Additional data related to this paper may be requested from the corresponding author upon request.

Acknowledgements

This work was financially supported by the National Natural Science Foundation of China (Nos. 52402315, 52372234, 22579147, and 22579146), Central Government Guided Local Science and

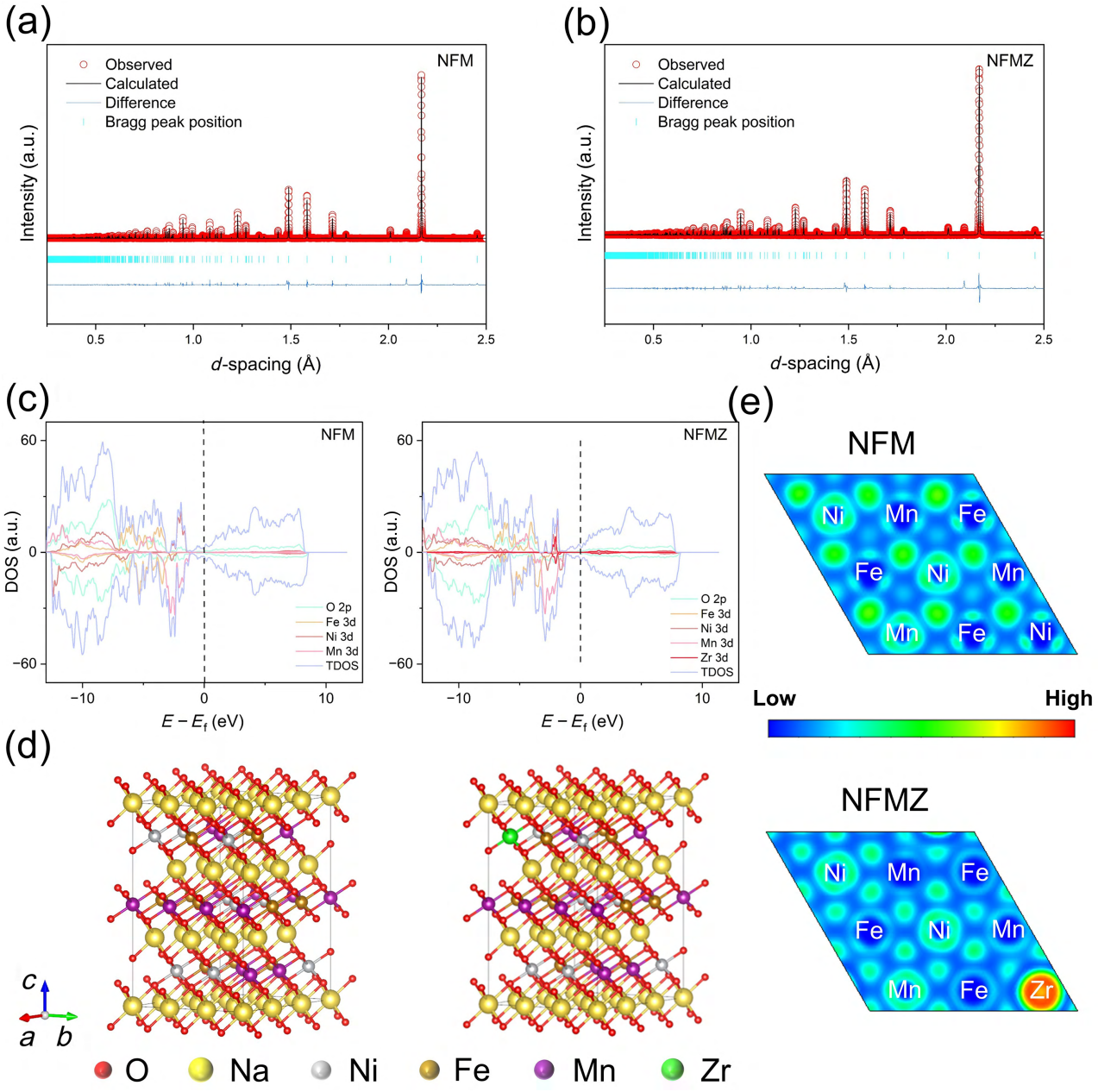


Figure 6 Neutron diffraction patterns of (a) NFM and (b) NFMZ cathode materials. (c) Density of states plot, (d) structure optimization diagram, and (e) ELF diagram of NFM and NFMZ.

Technology Development Project of Hebei Province (No. 246Z4409G), "Leading Innovative and Entrepreneur Team Introduction Program of Zhejiang" (No. 2023R01007), Zhejiang Provincial Natural Science Foundation of China (No. LQN25B030004), and the Natural Science Foundation of Sichuan Province (No. 2026NSFSC0082).

Declaration of competing interest

All the contributing authors report no conflict of interests in this work.

Author contribution statement

Z. X. L.: Data curation, writing – original draft, and formal analysis. J. G.: Data curation, formal analysis, and writing – original draft. Y. L. T.: Data curation and formal analysis. S. C. J.: Software and methodology. Z. C. X.: Data curation and formal analysis. L. B. W.: Investigation and funding acquisition. Z. H. L.: Project administration, funding acquisition, and writing – review & editing. M. H.: Formal analysis, writing – review & editing. W. L. C.: Resources, project administration, and funding acquisition. T. P. W.: Resuorces and funding acquisition. J. L.: Resources, project administration, and funding acquisition. J. X. S.: Conceptualization, funding acquisition, investigation, and writing – review & editing. All the authors have approved the final manuscript.

Use of AI statement

None.

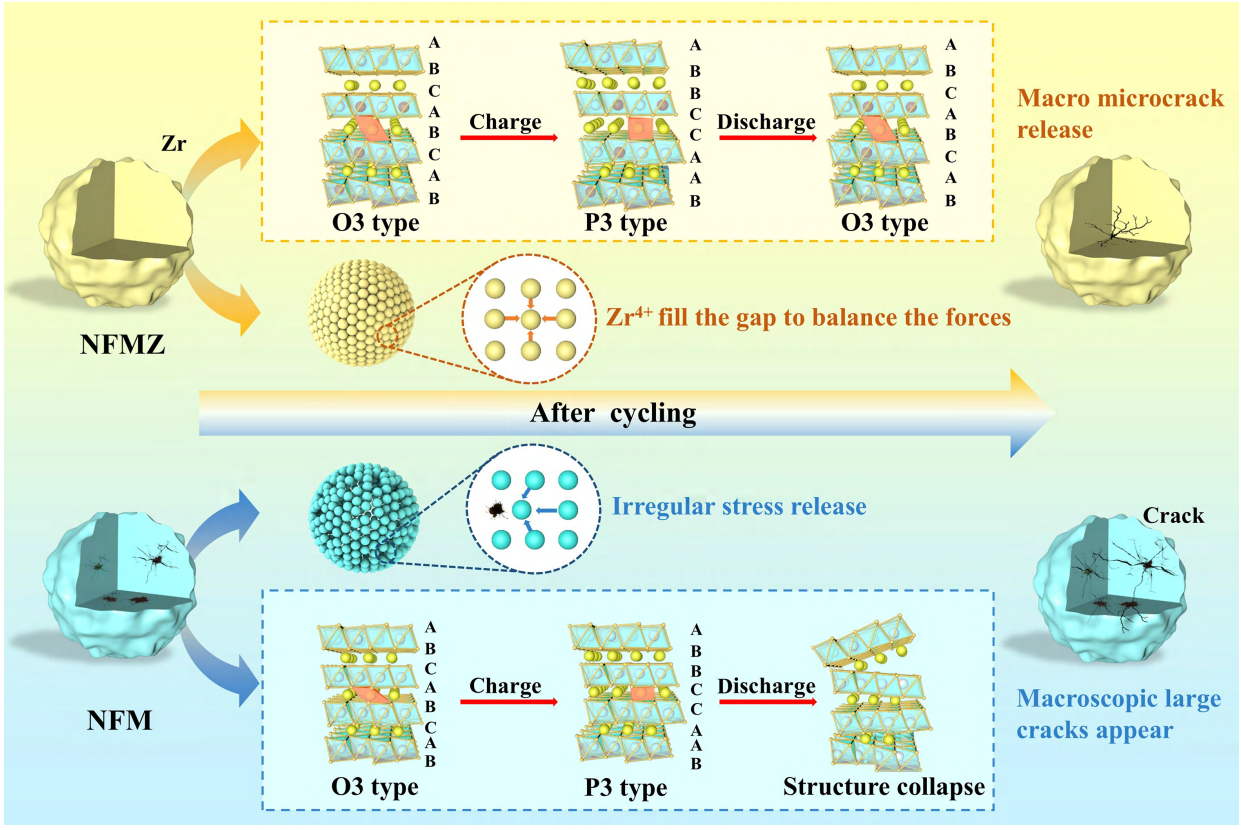


Figure 7 Schematic diagram of the mechanism for improving irregular stress release by Zr doping for the NFMZ cathode.

References

[1] Kang, Q.; Zhuang, Z. C.; Liu, Y. J.; Liu, Z. H.; Li, Y.; Sun, B.; Pei, F.; Zhu, H.; Li, H. F.; Li, P. L. et al. Engineering the structural uniformity of gel polymer electrolytes via pattern-guided alignment for durable, safe solid-state lithium metal batteries. *Adv. Mater.* **2023**, *35*, 2303460.

[2] Li, J. L.; Gan, T.; Yu, R. H.; Cai, J.; Zhuang, Z. C.; Zhu, H. Cooling crystallization at solid interfaces en route to a Janus nanocatalyst. *Adv. Mater.* **2026**, *38*, e12893.

[3] Xu, J.; Kang, Q.; Peng, B.; Zhuang, Z. C.; Wang, D. S.; Ma, L. B. Engineering single-atom catalysts for sulfur electrochemistry in metal–sulfur batteries. *J. Energy Chem.* **2025**, *106*, 768–790.

[4] Yang, X. H.; Yang, J. R.; Zheng, X. B.; Dou, Y. H.; Li, H. T.; Zhang, Y.; Li, Y. F.; Wang, D. S.; Yu, B.; Zhuang, Z. C. Enzyme-mimetic single-atom catalyst design for green ammonia synthesis. *Adv. Energy Mater.* **2025**, *15*, 2501867.

[5] Yang, X. H.; Liu, D.; Zhang, Y.; Fu, C.; Qiu, Z.; Li, Y. F.; Zhuang, Z. C.; Yu, B. An alkali-modified biochar-supported single-atom catalyst with enhanced mass transfer for efficient nitrate electrolysis. *Nano Res.* **2026**, *19*, 94908413.

[6] Liu, Y.; Xin, Y.; He, B. J.; Zhang, F.; Wang, C.; Tian, H. J. High entropy fine-tuning achieves fast Li^+ kinetics in high-performance Co-free high-Ni layered cathodes. *Adv. Mater.* **2025**, *37*, 2417353.

[7] Zhou, Y. H.; Zhao, M.; Bai, K.; Xu, X. M.; Wang, H. F.; Chen, Y.; Zeng, J.; Tong, H.; He, H. B. Research on the construction of high-stability O3-type sodium-ion battery cathode materials via B–Co doping based on solid solutions. *Chem. Eng. J.* **2025**, *512*, 161943.

[8] Xu, C. H. Y.; Jing, P.; Xia, P. F.; Jia, Y.; Peng, J. N.; He, Q. J.; Liu, Q. Q.; Song, Z. M.; Zhang, X. M.; Wu, F. L. et al. Tailoring a multilayer fine-grained solid electrolyte interphase by pulse electrochemical activation maneuver for stable Si/C anodes. *Energy Environ. Sci.* **2025**, *18*, 7060–7070.

[9] Tang, G. B.; Li, Y.; Wu, J. X.; Kang, Q.; Ma, L. B. Engineering heterostructured electrocatalysts for enhanced sulfur redox kinetics in metal–sulfur batteries. *Nano Res. Energy* **2025**, *4*, e9120179.

[10] He, Q. J.; Deng, Z. W.; Miao, S. C.; Jia, Y.; Peng, J.; Xia, P. F.; Xu, C. H. Y.; Tang, Q.; Zhang, X. M.; Tan, T. N. et al. An anion outer-regulated electrolyte allows rapid desolvation to enable high-voltage lithium metal batteries. *Energy Environ. Sci.* **2025**, *18*, 9093–9104.

[11] Lin, J. R.; Shi, X. Y.; Xu, J. L.; Shao, L. Y.; Sun, Z. P. Enabling accelerated Na^+ dynamics through Li-induced electrostatic shielding for high-performance $Na_3V_2(PO_4)_2F_3$ cathode. *Adv. Energy Mater.* **2025**, *15*, 2501979.

[12] Shi, C. L.; Muhtar, D.; Lu, X. Y.; Liu, F. Q.; Lu, X.; Sun, Z. P.; Guo, Z. P. A medium-entropy NASICON cathode for sodium-ion batteries achieving high energy density through dual enhancement of voltage and capacity. *Adv. Energy Mater.* **2025**, *15*, 2500448.

[13] Shi, C. L.; Muhtar, D.; Pei, Y. L.; Lu, X. Y.; Liu, F. Q.; Wang, D.; Lu, X.; Sun, Z. P. Suppressing V/Na anti-site defects via fluorine doping enables high-voltage and stable V-based NASICON cathodes for sodium-ion batteries. *Adv. Energy Mater.* **2026**, *16*, e70898.

[14] Shi, C. L.; Xu, J. L.; Tao, T.; Lu, X. Y.; Liu, G. P.; Xie, F. Q.; Wu, S.; Wu, Y. X.; Sun, Z. P. Zero-strain $Na_3V_2(PO_4)_2F_3$@Rgo/CNT composite as a wide-temperature-tolerance cathode for Na-ion batteries with ultrahigh-rate performance. *Small Methods* **2024**, *8*, 2301277.

[15] Wang, K.; Zhang, Z. F.; Cheng, S. L.; Han, X.; Fu, J. J.; Sui, M.; Yan, P. F. Precipitate-stabilized surface enabling high-performance $Na_{0.67}Ni_{0.33-x}Mn_{0.67}Zn_xO_2$ for sodium-ion battery. *eScience* **2022**, *2*, 529–536.

[16] Zhou, J. Y.; Qin, L. Y.; Fang, L.; Zhu, X. J.; Wang, L. L.; Zhuang, Z. C. 2M-phase transition metal dichalcogenides: From fundamental to application. *Nano Res.* **2025**, *18*, 94907312.

[17] Zhuang, Z. C.; Wang, D. S. Advancing hydrogen energy through enzyme-mimetic electrocatalysis. *Front. Energy* **2025**, *19*, 563–567.

[18] Wang, P. F.; You, Y.; Yin, Y. X.; Guo, Y. G. Layered oxide cathodes

for sodium-ion batteries: Phase transition, air stability, and performance. *Adv. Energy Mater.* **2018**, *8*, 1701912.

[19] Goikolea, E.; Palomares, V.; Wang, S. J.; De Larramendi, I. R.; Guo, X.; Wang, G. X.; Rojo, T. Na-ion batteries—Approaching old and new challenges. *Adv. Energy Mater.* **2020**, *10*, 2002055.

[20] Joshi, A.; Chakrabarty, S.; Akella, S. H.; Saha, A.; Mukherjee, A.; Schmerling, B.; Ejgenberg, M.; Sharma, R.; Noked, M. High-entropy Co-free O3-type layered oxyfluoride: A promising air-stable cathode for sodium-ion batteries. *Adv. Mater.* **2023**, *35*, 2304440.

[21] Xu, Z. W.; Song, K. W.; Chang, X. Y.; Li, L.; Zhang, W. C.; Xue, Y. X.; Zhang, J. H.; Lin, D. W.; Liu, Z. Y.; Wang, Q. et al. Layered oxide cathodes: A comprehensive review of characteristics, research, and development in lithium and sodium ion batteries. *Carbon Neutralizat.* **2024**, *3*, 832–856.

[22] Zhang, T.; Ren, M.; Huang, Y. H.; Li, F.; Hua, W. B.; Indris, S.; Li, F. J. Negative lattice expansion in an O3-type transition-metal oxide cathode for highly stable sodium-ion batteries. *Angew. Chem., Int. Ed.* **2024**, *63*, e202316949.

[23] Yao, J.; Wang, X. S.; Hu, P.; Fan, J. H.; Yang, X. P.; Jiang, W. H.; Jiang, S. W.; Dong, P.; Zhang, Y. J.; Duan, J. G. et al. Local Electron spin-state modulation at Mn site for advanced sodium-ion batteries with fast-kinetic $NaNi_{0.33}Fe_{0.33}Mn_{0.33}O_2$ cathode. *Adv. Funct. Mater.*, in press, DOI: 10.1002/adfm.202419967.

[24] Zhou, D. M.; Zeng, C.; Xiang, J.; Wang, T.; Gao, Z. T.; An, C. L.; Huang, W. X. Review on Mn-based and Fe-based layered cathode materials for sodium-ion batteries. *Ionics* **2022**, *28*, 2029–2040.

[25] Li, M.; Zhuo, H. X.; Lei, J. W.; Guo, Y. Q.; Yuan, Y. F.; Wang, K.; Liao, Z.; Xia, W.; Geng, D. S.; Sun, X. L. et al. Unravelling the structure–stability interplay of O3-type layered sodium cathode materials via precision spacing engineering. *Nat. Commun.* **2025**, *16*, 2010.

[26] Li, L. C.; Liu, T. T.; Ding, M. H.; Yu, H. H.; Dou, Z. A.; Wang, L. X.; Weng, J. Y.; Wu, X. Z.; Zhou, J.; Zhou, P. F. Structural modulation for ultrastable O3-type layered oxide cathode material of sodium-ion batteries. *Adv. Funct. Mater.* **2025**, *36*, e14832.

[27] Ding, F. X.; Zhao, C. L.; Zhou, D.; Meng, Q. S.; Xiao, D. D.; Zhang, Q. Q.; Niu, Y. S.; Li, Y. Q.; Rong, X. H.; Lu, Y. X. et al. A novel Ni-rich O3-$Na[Ni_{0.60}Fe_{0.25}Mn_{0.15}]O_2$ cathode for Na-ion batteries. *Energy Storage Mater.* **2020**, *30*, 420–430.

[28] Zou, Y. G.; Mao, H. C.; Meng, X. H.; Du, Y. H.; Sheng, H.; Yu, X. Q.; Shi, J. L.; Guo, Y. G. Mitigating the kinetic hindrance of single-crystalline Ni-rich cathode via surface gradient penetration of tantalum. *Angew. Chem., Int. Ed.* **2021**, *60*, 26535–26539.

[29] Liang, X. H.; Song, X. S.; Sun, H. H.; Kim, H.; Kim, M. C.; Sun, Y. K. High-energy and long-life O3-type layered cathode material for sodium-ion batteries. *Nat. Commun.* **2025**, *16*, 3505.

[30] Yang, J.; Liang, X. H.; Ryu, H. H.; Yoon, C. S.; Sun, Y. K. Ni-rich layered cathodes for lithium-ion batteries: From challenges to the future. *Energy Storage Mater.* **2023**, *63*, 102969.

[31] Gao, Z. Y.; Zhao, C. L.; Zhou, K.; Wu, J. R.; Tian, Y.; Deng, X. M.; Zhang, L. H.; Lin, K.; Kang, F. Y.; Peng, L. L. et al. Kirkendall effect-induced uniform stress distribution stabilizes nickel-rich layered oxide cathodes. *Nat. Commun.* **2024**, *15*, 1503.

[32] Zhou, W.; Li, S. H.; Jin, R.; Zhang, Y.; Gao, X. G.; Li, J.; Lai, Y. Q.; Zhang, Z. A. Surface structure reconstruction to suppress heterogeneous phase transformation for air-stable single crystalline O3-type sodium oxide. *Energy Storage Mater.* **2025**, *74*, 103881.

[33] Li, M.; Zhuo, H. X.; Song, M.; Gu, Y.; Yang, X.; Li, C. X.; Liao, Z.; Ye, Y. H.; Zhao, C. T.; Jiang, Y. Y. et al. Tailoring Cu-rich surface spinel phase for high-performance O3-type layered cathode materials for sodium-ion batteries. *Nano Energy* **2024**, *123*, 109375.

[34] Feng, S.; Lu, Y.; Lu, X. Y.; Chen, H.; Wu, X. W.; Wu, M. F.; Xu, F. F.; Wen, Z. Y. Surface engineering through *in situ* construction of Co_xB-spinel dual coating layers for high-voltage stable sodium-ion batteries. *Adv. Energy Mater.* **2024**, *14*, 2303773.

[35] Liang, X. H.; Yu, T. Y.; Ryu, H. H.; Sun, Y. K. Hierarchical O3/P2 heterostructured cathode materials for advanced sodium-ion batteries. *Energy Storage Mater.* **2022**, *47*, 515–525.

[36] Wang, J. E.; Kim, H.; Jung, Y. H.; Kim, D. K.; Kim, D. J. Designing high energy sodium-ion battery cathodes by utilizing P2/O3 biphasic structure and lithium honeycomb ordering. *Small* **2021**, *17*, 2100146.

[37] Nie, Z.; Liu, C.; Lai, Q. S.; Li, W.; Li, Q.; Yang, R.; Gao, X. W.; Gu, Q. F.; Luo, W. B. Constructing multiphase junction towards layer-structured cathode material for enhanced sodium ion batteries. *Energy Storage Mater.* **2025**, *74*, 103971.

[38] Liu, R. Y.; Yang, S. J.; Zhou, S. T.; Xing, J. X.; Niu, X. W.; Pang, G. Y.; Liu, G. C.; Ye, F.; Xiao, B. W.; Xu, C. Regulating reversible phase transition at high voltage window on O3-type layered cathodes by doping Zn for sodium-ion batteries. *Small* **2025**, *21*, e05197.

[39] Liu, X. Y.; Li, S.; Zhu, Y. F.; Zhang, X. Y.; Su, Y.; Li, M. Y.; Li, H. W.; Chen, B. B.; Liu, Y. F.; Xiao, Y. Promoting layered oxide cathodes based on structural reconstruction for sodium-ion batteries: Reversible phase transition, stable interface regulation, and multifunctional intergrowth structure. *Adv. Funct. Mater.* **2025**, *35*, 2414130.

[40] Zhang, K.; Xu, Z. M.; Li, G. D.; Luo, R. J.; Ma, C.; Wang, Y. G.; Zhou, Y. N.; Xia, Y. Y. Regulating phase transition and oxygen redox to achieve stable high-voltage O3-type cathode materials for sodium-ion batteries. *Adv. Energy Mater.* **2023**, *13*, 2302793.

[41] Guo, Y. J.; Wang, P. F.; Niu, Y. B.; Zhang, X. D.; Li, Q. H.; Yu, X. Q.; Fan, M.; Chen, W. P.; Yu, Y.; Liu, X. F. et al. Boron-doped sodium layered oxide for reversible oxygen redox reaction in Na-ion battery cathodes. *Nat. Commun.* **2021**, *12*, 5267.

[42] Gabriel, E.; Wang, P. B.; Graff, K.; Kelly, S. D.; Sun, C. J.; Deng, C. J.; Hwang, I.; Liu, J.; Li, C.; Kuraitis, S. et al. The role of Li doping in layered/layered $Na_xLi_yNi_{0.4}Fe_{0.2}Mn_{0.4}O_2$ intergrowth electrodes for sodium ion batteries. *Nano Energy* **2025**, *134*, 110556.

[43] Wen, X. Y.; Yang, C.; Fang, Z. Y.; Zhong, C. N.; Ou, J. K. High-rate Mg doped $NaNi_{1/3}Fe_{1/3}Mn_{1/3}O_2$ cathode with excellent low-temperature stability improved by one-step coprecipitation for sodium ion battery applications. *Chem. Eng. J.* **2025**, *522*, 167832.

[44] Wang, P. F.; Yao, H. R.; Liu, X. Y.; Zhang, J. N.; Gu, L.; Yu, X. Q.; Yin, Y. X.; Guo, Y. G. Ti-substituted $NaNi_{0.5}Mn_{0.5-x}Ti_xO_2$ cathodes with reversible O3–P3 phase transition for high-performance sodium-ion batteries. *Adv. Mater.* **2017**, *29*, 1700210.

[45] Huang, Z. X.; Long, Z.; Li, C.; Liu, K.; Zhang, Q. Q.; Liu, S. Q.; Guo, Y. Y.; Sun, W. L.; Mu, W. Y.; Shi, X. X. et al. Deciphering the function mechanism of high-valence tantalum doping in O3-types layered cathode for sodium-ion battery. *J. Energy Chem.* **2026**, *112*, 742–751.

[46] Lv, Y.; Huang, S. F.; Zhang, J. H.; Kang, G. H.; Liu, Y. R.; Li, N. R.; Liang, Y. X.; Zhong, X. Y.; Jia, T. Q.; Ouyang, Y. F. et al. Antimony doping enabled radially aligned microstructure in $LiNi_{0.91}Co_{0.06}Al_{0.03}O_2$ cathode for high-voltage and low-temperature lithium battery. *Adv. Funct. Mater.* **2024**, *34*, 2312284.

[47] Kim, D.; Lee, E.; Slater, M.; Lu, W. Q.; Rood, S.; Johnson, C. S. Layered $Na[Ni_{1/3}Fe_{1/3}Mn_{1/3}]O_2$ cathodes for Na-ion battery application. *Electrochem. Commun.* **2012**, *18*, 66–69.

[48] Liu, G. L.; Xu, W. L.; Wu, J. H.; Li, Y.; Chen, L. P.; Li, S. Y.; Ren, Q. H.; Wang, J. Unlocking high-rate O3 layered oxide cathode for Na-ion batteries via ion migration path modulation. *J. Energy Chem.* **2023**, *83*, 53–61.

[49] Wang, X. T.; Zhang, Q. H.; Zhao, C.; Li, H. F.; Zhang, B. D.; Zeng, G. F.; Tang, Y. L.; Huang, Z. Y.; Hwang, I.; Zhang, H. T. et al. Achieving a high-performance sodium-ion pouch cell by regulating intergrowth structures in a layered oxide cathode with anionic redox. *Nat. Energy* **2024**, *9*, 184–196.

[50] Xie, C. L.; Liu, S. F.; Wang, J.; Meng, X. H.; Yu, S. Y.; Zhang, J. N.; Peng, H. J.; Sun, D.; Tang, Y. G.; Wang, H. Y. Sodium-compensating electrolyte additives stabilize interfaces for highly reversible anode-free sodium batteries. *Energy Environ. Sci.* **2026**, *19*, 200–210.

[51] Chen, Z. G.; Li, Z. H.; Ying, Y. R.; Shen, C.; Chen, S.; Xie, K. Y. Electric field-driven competitive ionic-molecular coordination in the

helmholtz plane enables high-voltage and high-temperature sodium-ion batteries. *J. Am. Chem. Soc.* **2026**, *148*, 7532–7543.

[52] Zhao, S. Y.; Ning, F. H.; Yu, X.; Guo, B. Y.; Teófilo, R. F.; Huang, J. Y.; Shi, Q. H.; Wu, S.; Feng, W. L.; Zhao, Y. F. Inhomogeneous coordination in high-entropy O3-type cathodes enables suppressed slab gliding and durable sodium storage. *Angew. Chem., Int. Ed.* **2025**, *64*, e202416290.

[53] Maddar, F. M.; Gonos, K.; Singh, M.; Compton, J.; Atkinson, D.; Capener, M. J.; Copley, M.; Hasa, I. Upscaling sodium-ion battery cells: From aqueous processing to performance assessment of hard carbon|Prussian white pouch cells. *Adv. Energy Mater.*, in press, DOI: 10.1002/aenm.202505344.

[54] Dong, P. Y.; Peng, F.; Zhang, Q. M.; Wang, H.; Chu, Y. Q.; Chen, C. D.; Yang, C. H. High entropy boosts the low temperature Na^+-storage performance of $Na_4Fe_3(PO_4)_2P_2O_7$. *Angew. Chem., Int. Ed.* **2025**, *64*, e202502693.

[55] Zou, Z. Y.; Mu, Y. B.; Han, M. S.; Chu, Y. Q.; Liu, J.; Zheng, K. X.; Zhang, Q.; Song, M. R.; Jian, Q. P.; Wang, Y. L. et al. Integrated polyanion-layered oxide cathodes enabling 100 000 cycle life for sodium-ion batteries. *Energy Environ. Sci.* **2025**, *18*, 2216–2230.

[56] Huang, Y. C.; Gu, S.; Xu, X.; An, Z. B.; Han, X. D.; Cao, Y. L.; He, D. S.; Zhang, F. C.; Guo, H.; Liu, Y. et al. Negative enthalpy doping stabilizes P2-type oxides cathode for high-performance sodium-ion batteries. *Adv. Mater.* **2025**, *37*, 2408012.

[57] Huang, P.; Lin, J. L.; Wang, Z. A.; Li, W. J.; Chen, Y. J.; Zhou, L. J.; Chen, L. B.; Zhang, C. X.; Wei, W. F. Competitive solvation structures via hetero-salt additive strategy enables temperature-adaptive sodium-ion batteries. *Adv. Funct. Mater.* **2025**, *35*, 2413302.

[58] Feng, X. C.; Li, Y.; Shi, Q. H.; Wang, X.; Yin, X. P.; Wang, J.; Xia, Z. H.; Xiao, H. Y.; Chen, A. B.; Yang, X. X. et al. A comprehensive modification enables the high rate capability of P2-$Na_{0.75}Mn_{0.67}Ni_{0.33}O_2$ for sodium-ion cathode materials. *J. Energy Chem.* **2022**, *69*, 442–449.

[59] Yu, T. Y.; Sun, Y. K. A fluorinated O3-type layered cathode for long-life sodium-ion batteries. *J. Mater. Chem. A.* **2022**, *10*, 23639–23648.

[60] Chen, J.; Zou, G. Q.; Deng, W. T.; Huang, Z. D.; Gao, X.; Liu, C.; Yin, S. Y.; Liu, H. Q.; Deng, X. L.; Tian, Y. et al. Pseudo-bonding and electric-field harmony for Li-rich Mn-based oxide cathode. *Adv. Funct. Mater.* **2020**, *30*, 2004302.

[61] Sun, C. C.; Chen, J. R.; Hou, H. H.; Kong, F. J.; Wu, D. J.; Cui, P. X.; Zhang, L.; Tao, S. Covalency regulation of metal-oxygen ligand in O3-type layered cathode material for high-performance sodium-ion batteries. *Energy Storage Mater.* **2026**, *84*, 104820.

This is an open access article under the terms of the Creative Commons Attribution 4.0 International License (CC BY 4.0, https://creativecommons.org/licenses/by/4.0/).

© The Author(s) 2026. Published by Tsinghua University Press.